

nIFTy galaxy cluster simulations – V. Investigation of the cluster infall region

Jake Arthur,^{1*} Frazer R. Pearce,¹ Meghan E. Gray,¹ Pascal J. Elahi,^{2,3}
 Alexander Knebe,^{4,5} Alexander M. Beck,⁶ Weiguang Cui,^{3,7} Daniel Cunnama,^{8,9}
 Romeel Davé,^{8,9,10} Sean February,¹¹ Shuiyao Huang,¹² Neal Katz,¹² Scott T. Kay,¹³
 Ian G. McCarthy,¹⁴ Giuseppe Murante,¹⁵ Valentin Perret,¹⁶ Chris Power,^{3,7}
 Ewald Puchwein,¹⁷ Alexandro Saro,¹⁸ Federico Sembolini,^{4,5} Romain Teyssier¹⁹
 and Gustavo Yepes^{4,5}

Affiliations are listed at the end of the paper

Accepted 2016 September 22. Received 2016 September 14; in original form 2016 April 29

ABSTRACT

We examine the properties of the galaxies and dark matter haloes residing in the cluster infall region surrounding the simulated Λ cold dark matter galaxy cluster studied by Elahi et al. at $z = 0$. The $1.1 \times 10^{15} h^{-1} M_{\odot}$ galaxy cluster has been simulated with eight different hydrodynamical codes containing a variety of hydrodynamic solvers and sub-grid schemes. All models completed a dark-matter-only, non-radiative and full-physics run from the same initial conditions. The simulations contain dark matter and gas with mass resolution $m_{\text{DM}} = 9.01 \times 10^8 h^{-1} M_{\odot}$ and $m_{\text{gas}} = 1.9 \times 10^8 h^{-1} M_{\odot}$, respectively. We find that the synthetic cluster is surrounded by clear filamentary structures that contain ~ 60 per cent of haloes in the infall region with mass $\sim 10^{12.5} - 10^{14} h^{-1} M_{\odot}$, including 2–3 group-sized haloes ($> 10^{13} h^{-1} M_{\odot}$). However, we find that only ~ 10 per cent of objects in the infall region are sub-haloes residing in haloes, which may suggest that there is not much ongoing pre-processing occurring in the infall region at $z = 0$. By examining the baryonic content contained within the haloes, we also show that the code-to-code scatter in stellar fraction across all halo masses is typically ~ 2 orders of magnitude between the two most extreme cases, and this is predominantly due to the differences in sub-grid schemes and calibration procedures that each model uses. Models that do not include active galactic nucleus feedback typically produce too high stellar fractions compared to observations by at least ~ 1 order of magnitude.

Key words: methods: numerical – galaxies: clusters: general – dark matter.

1 INTRODUCTION

In the Λ cold dark matter (Λ CDM) paradigm, galaxy clusters are built hierarchically by accreting smaller objects from the cluster infall region (Springel et al. 2005), which we define here as the volume outside the galaxy cluster’s virial radius. As galaxies fall into a cluster, their internal properties are significantly affected by their local environment, an effect that is more apparent nearer the overdense cluster centre (Dressler 1980; Lewis et al. 2002; Gómez et al. 2003; Hogg et al. 2004; Poggianti et al. 2006; Bamford et al. 2009). Here, several physical mechanisms are thought to quench

a galaxy’s star formation or alter its morphology as it infalls (for review see Boselli & Gavazzi 2006).

In the cluster centre, it is difficult to disentangle these mechanisms, but by studying objects in the infall region we can not only examine what is building these clusters, but also possibly break this degeneracy. However, understanding cluster-specific phenomena is not the only reason to study the infall region of a galaxy cluster. Many observational and theoretical studies have now raised the question of how important *pre-processing* is, whereby some physical process is able to initiate significant changes as galaxies fall into groups and filaments well outside the virial region (Fujita 2004; McGee et al. 2009; Bahé et al. 2013; Cybulski et al. 2014). However, pre-processing can be observationally difficult to study due to contamination from backsplash galaxies, which are galaxies that have already entered the cluster core, undergone significant

* E-mail: jake.arthur@nottingham.ac.uk

disruption and travelled back out to the cluster outskirts. In fact, by using dark-matter-only (DM-only) simulations Gill, Knebe & Gibson (2005) found that ~ 50 per cent of galaxies residing between R_{200} and $2R_{200}$ of the main cluster halo are backsplash galaxies.

Hydrodynamical simulations are now vital tools in aiding and interpreting astronomical observations of galaxy clusters (Borgani & Kravtsov 2011), enabling us to track and quantify environmental effects as galaxies fall into the cluster. For example, Bahé & McCarthy (2015) used the GIMIC simulations (Crain et al. 2009) to track galaxies falling into groups and clusters in order to understand the characteristic time-scales of each environmental quenching mechanism and in what environment each dominated. Simulations are therefore invaluable for studying pre-processing in the cluster infall region, but before concrete conclusions can be drawn, the validity of simulations must be checked.

Hydrodynamical simulations model dark matter (DM) and gas coupled together through gravity, and evolve gas with the hydrodynamic equations. These equations are typically solved with either Lagrangian smoothed particle hydrodynamics (SPH; Gingold & Monaghan 1977; Lucy 1977; Springel 2010a) or Eulerian mesh-based schemes with optional adaptive mesh refinement (AMR; Cen & Ostriker 1992; Stone & Norman 1992; Kravtsov, Klypin & Khokhlov 1997; Teyssier 2002). The most famous comparison between state-of-the-art codes employing these numerical schemes was The Santa Barbara Cluster Comparison Project in Frenk et al. (1999). This study showed that mesh-based codes produced a simulated galaxy cluster with a cored entropy profile, which was worryingly absent in the SPH codes.

Since then, more comparison studies have gone on to highlight other problems inherent in each numerical scheme. SPH methods typically have low shock resolution, poor accuracy in the treatment of contact discontinuities and they have been shown to suppress fluid instabilities (Agertz et al. 2007). In addition, Eulerian mesh schemes are not strictly Galilean invariant, making the results sensitive to bulk velocities (Tasker et al. 2008), which is particularly concerning for simulations of galaxy formation. More recently, hybrid schemes and improved SPH schemes have been developed to account for these problems (Read, Hayfield & Agertz 2010; Springel 2010b; Hopkins et al. 2014).

On the other hand, the baryonic physics governing galaxy formation still remains uncertain, and including it complicates the simulations further. The focus has now shifted to creating simulations that are able to reproduce realistic galaxies (Vogelsberger et al. 2014; Schaye et al. 2015). The idea is to model the cooling and radiative physics that occurs as gas is converted into stars, and as feedback drives powerful outflows. More specifically, codes are now trying to model galaxy formation by including processes such as gas cooling (e.g. Pearce et al. 2000; Wiersma, Schaye & Smith 2009), formation of stars from overdense gas (e.g. Springel & Hernquist 2003; Schaye & Dalla Vecchia 2008), injection of energy from supernova (e.g. Dalla Vecchia & Schaye 2012), growth of black holes (e.g. Di Matteo, Springel & Hernquist 2005) and outflows from active galactic nucleus (AGN) accretion (e.g. Booth & Schaye 2009). Because of the large range of spatial and temporal scales that these mechanisms cover, they are simplified with analytical prescriptions containing tunable free parameters, namely *sub-grid* physics. These sub-grid prescriptions still remain the largest uncertainties in galaxy formation simulations, with each simulation using its own preferred analytical prescriptions and calibrating the free parameters differently.

The problems that plague modern galaxy formation simulations have prompted a rise in important comparison studies such

as AQUILA and AGORA (Scannapieco et al. 2012; Kim et al. 2014). Projects such as these have investigated simulated galaxies resulting from different combinations of hydrodynamic solvers, sub-grid schemes and resolution. This paper is a continuation of one such study, the *nIFTy cluster comparison project*. In the nIFTy cluster comparison series, we use several different SPH and mesh codes, each equipped with its own preferred and calibrated sub-grid schemes, to study the formation and evolution of a large $M_{200} = 1.1 \times 10^{15} h^{-1} M_{\odot}$ galaxy cluster produced by each code. The largest objects within the background DM distributions between all codes have been sufficiently aligned following a prescription described in Paper I (Sembolini et al. 2016a), allowing a robust comparison to be carried out between hydrodynamic solvers and sub-grid prescriptions included in each code. Also, by focusing on a simulated galaxy cluster, we can compare different codes in a variety of overdensities with a statistically robust sample of haloes.

Because of recent improvements in SPH and mesh-based hydrodynamic solvers, the initial paper in the nIFTy series (Sembolini et al. 2016a) revisited the work done in Frenk et al. (1999) by examining the bulk properties of the simulated galaxy cluster at $z = 0$ in both DM-only and non-radiative (NR; including gas but not cooling) runs. They found there was very good agreement in the DM density profiles between all codes, but the scatter in gas density profiles was of order a factor of ~ 2 . Most importantly, they found that the codes that employed a modern SPH scheme were able to reproduce an entropy core seen in the mesh-based codes.

Paper II (Sembolini et al. 2016b) analysed the effect the inclusion of full radiative baryonic physics had on the bulk properties of the simulated cluster at $z = 0$. When including the uncertain baryonic physics, they found there is significantly more scatter in the bulk properties between codes in the full-physics (FP) run compared to the NR run. The entropy profiles were also strongly affected by the radiative processes and washed out any differences between classic and modern SPH. Since then, Cui et al. (2016) focused on the effect of including baryons on the galaxy cluster mass and kinematic profiles, as well as global measures of the cluster (e.g. mass, concentration, spin and shape). They found a good consistency ($\lesssim 20$ per cent) between global properties of the cluster predicted by different codes when integrated quantities are measured within the virial radius R_{200} . However, there are larger differences for quantities within R_{2500} .

In Paper III, Elahi et al. (2016, hereafter E16) analysed the sub-haloes and galaxies produced by each code inside the central $1.8 h^{-1}$ Mpc region surrounding the cluster. Whilst the code-to-code scatter in sub-halo abundance was low in the DM-only and NR runs (codes differed by up to a factor of 1.3 and 1.9, respectively), the scatter was amplified in the FP run when the sub-grid physics was included. Here codes differed by up to a factor of ~ 2.4 . The discrepancy between codes in galaxy abundance is even worse: differences here extended up to a factor of 20 between the most extreme cases.

We would expect the code-to-code scatter in E16 to be mainly attributable to the different sub-grid prescriptions and calibration methods each code uses. However, in the overdense centre differences in the gas environments are largest due to different hydro solvers and sub-grid schemes between the models, and this could potentially have a sizeable effect on the code-to-code scatter seen in the central region. Therefore, this begs the question: in E16 do the differences in the sub-grid schemes dominate the code-to-code scatter and how much is due to the different gas environments in which the haloes and galaxies live? To investigate this, we have extended the work done in E16 by studying the simulated galaxy cluster infall region at $z = 0$. By using objects within a sphere of

Table 1. A brief summary of the models used in this study specifying which ones include stellar (SN) and AGN feedback.

Type	Model	SN	AGN
AMR	RAMSES	✗	✓
Moving Mesh	AREPO-IL	✓	✓
	AREPO-SH	✓	✗
Classic SPH	G3-MUSIC	✓	✗
	G3-MUSICPI	✓	✗
	G3-OWLS	✓	✓
Modern SPH	G2-X	✓	✓
	G3-X	✓	✓
	G3-PESPH	✓	✗
	G3-MAGNETICUM	✓	✓

radius $5 h^{-1}$ Mpc centred on the cluster centre of mass, we have investigated whether the code-to-code scatter persists out to the less overdense infall region and how well each participating code can match to observed stellar and gas fractions. Also, by studying the infall region, we may investigate what is currently building our synthetic cluster.

The paper is organized as follows. In Section 2, we briefly describe the participating codes, the simulated galaxy cluster and how we produced our halo catalogues. We present our results in Section 3. Section 4 contains a discussion along with our conclusions.

2 NUMERICAL METHODS

2.1 Codes

In this study, we compare eight state-of-the-art hydrodynamical codes that contain calibrated subgrid physics. These include one adaptive mesh refinement code, RAMSES, the moving mesh code, AREPO, and six variants of the SPH code GADGET, G3-MAGNETICUM, G3-X, G3-PESPH, G3-MUSIC, G3-OWLS and G2-X. An extensive summary of how each code solves the hydrodynamic equations is presented in Paper I of the *nIFTy* series.

Each code incorporates its own preferred sub-grid schemes for dealing with gas cooling/heating, star formation and feedback, stellar population properties and chemistry and SMBH growth and AGN feedback; the details of which are included in Paper II and are also summarized in table 1 in E16. For ease, we have also included a brief summary of the participating models in Table 1. We note that RAMSES employs thermal AGN feedback and no stellar feedback to moderate cooling (Teyssier 2002; Teyssier et al. 2011). AREPO has been run twice with variant sub-grid physics, one including AGN feedback (AREPO-IL) and one not including it (AREPO-SH; Vogelsberger et al. 2013, 2014). AREPO-SH is not a production code and has only been included in this study to observe the effect of switching off AGN feedback. G3-MUSIC includes no AGN feedback and only moderates cooling using stellar feedback based on Springel & Hernquist (2003, hereafter SH03) (Sembolini et al. 2013). A second variant of G3-MUSIC has been run, G3-MUSICPI, with modified kinetic feedback described in Piontek & Steinmetz (2011). G3-PESPH does not include AGN feedback, but uses a SH03 stellar feedback scheme with additional quenching in massive galaxies based on Rafieferantsoa et al. (2015) (Huang et al., in preparation). G3-OWLS (Schaye et al. 2010), G2-X (Pike et al. 2014), G3-X (Beck et al. 2016) and G3-MAGNETICUM (Hirschmann et al. 2014) all employ some combination of stellar feedback and thermal AGN.

2.2 Data

We use an $M_{200} = 1.1 \times 10^{15} h^{-1} M_{\odot}$ galaxy cluster drawn from the MUSIC-2 catalogue (Sembolini et al. 2013, 2014; Biffi et al. 2014), which is a mass-limited sample of resimulated haloes selected from the MultiDark DM-only cosmological simulation (Prada et al. 2012). The MultiDark simulation contains 2048^3 particles in a cube with side length $1 h^{-1}$ Gpc, where the chosen cosmology corresponds to the best-fitting Λ CDM model to 7-year *Wilkinson Microwave Anisotropy Probe* (WMAP7)+baryon acoustic oscillations (BAO)+Type I supernova (SNI) data with cosmological parameters taking the values $\Omega_m = 0.27$, $\Omega_b = 0.0469$, $\Omega_{\Lambda} = 0.73$, $\sigma_8 = 0.82$, $n = 0.95$ and $h = 0.7$ (Komatsu et al. 2011). All the data from the MultiDark simulation are publicly available online through the MultiDark data base.¹

The MUSIC-2 cluster catalogue was constructed by selecting all objects in the MultiDark volume with mass $> 10^{14} h^{-1} M_{\odot}$ at $z = 0$. These haloes were then resimulated using a zooming technique described in Klypin et al. (2001). In a low-resolution (256^3) MultiDark volume, particles in a sphere of radius $6 h^{-1}$ Mpc around each selected object were mapped back to their initial conditions. These initial conditions from the original simulations were then generated on a 4096^3 size mesh, improving the mass resolution of the resimulated haloes by a factor of 8. Each code completed a DM-only, NR and FP run. The mass resolution of particles in the particle-based codes in the DM-only simulations is $m_{\text{DM}} = 1.09 \times 10^9 h^{-1} M_{\odot}$ and in the gas runs is $m_{\text{DM}} = 9.01 \times 10^8 h^{-1} M_{\odot}$ and $m_{\text{gas}} = 1.9 \times 10^8 h^{-1} M_{\odot}$. The grid resolution in the mesh codes was chosen to match these particle resolutions as shown in Sembolini et al. (2016a).

2.3 Analysis

2.3.1 Halo catalogues

All haloes and sub-haloes were identified and analysed using VELOCIRAPTOR (also known as STF; Elahi, Thacker & Widrow 2011, freely available <https://github.com/pelahi/VELOCIRaptor-STF.git>), which identifies haloes using a 3D friends-of-friends (FOF) algorithm and then identifies sub-haloes using a phase-space FOF algorithm. In this paper, a sub-halo is a self-bound satellite object within the virial radius of another larger halo. Both haloes and sub-haloes are identified by only considering DM particles. VELOCIRAPTOR identifies self-bound structures as haloes or sub-haloes once they contain a minimum of 20 particles. In our simulations, bound baryonic particles are associated with the halo or sub-halo of the closest DM particle. As in E16, a galaxy in this study is defined as any self-bound structure that contains 20 or more star particles, corresponding to a galaxy mass of $\sim 2 \times 10^9 h^{-1} M_{\odot}$.

2.3.2 Contaminant removal

In this paper, we study all objects within a sphere of radius $5 h^{-1}$ Mpc centred on the cluster centre of mass at $z = 0$. As this is a zoom simulation with a nested hierarchy of progressively lower mass resolution shells, it is possible for low-resolution DM ‘interloper’ particles to enter into the region of interest from the low-resolution outskirts. We have traced these particles, and in all of our simulations we find ~ 20 interloper particles in the infall region, lying in two groups. We have removed all of the haloes lying within $1 h^{-1}$ Mpc of these groups from our analysis. Only ~ 30 haloes are excluded

¹ <https://www.cosmosim.org/>

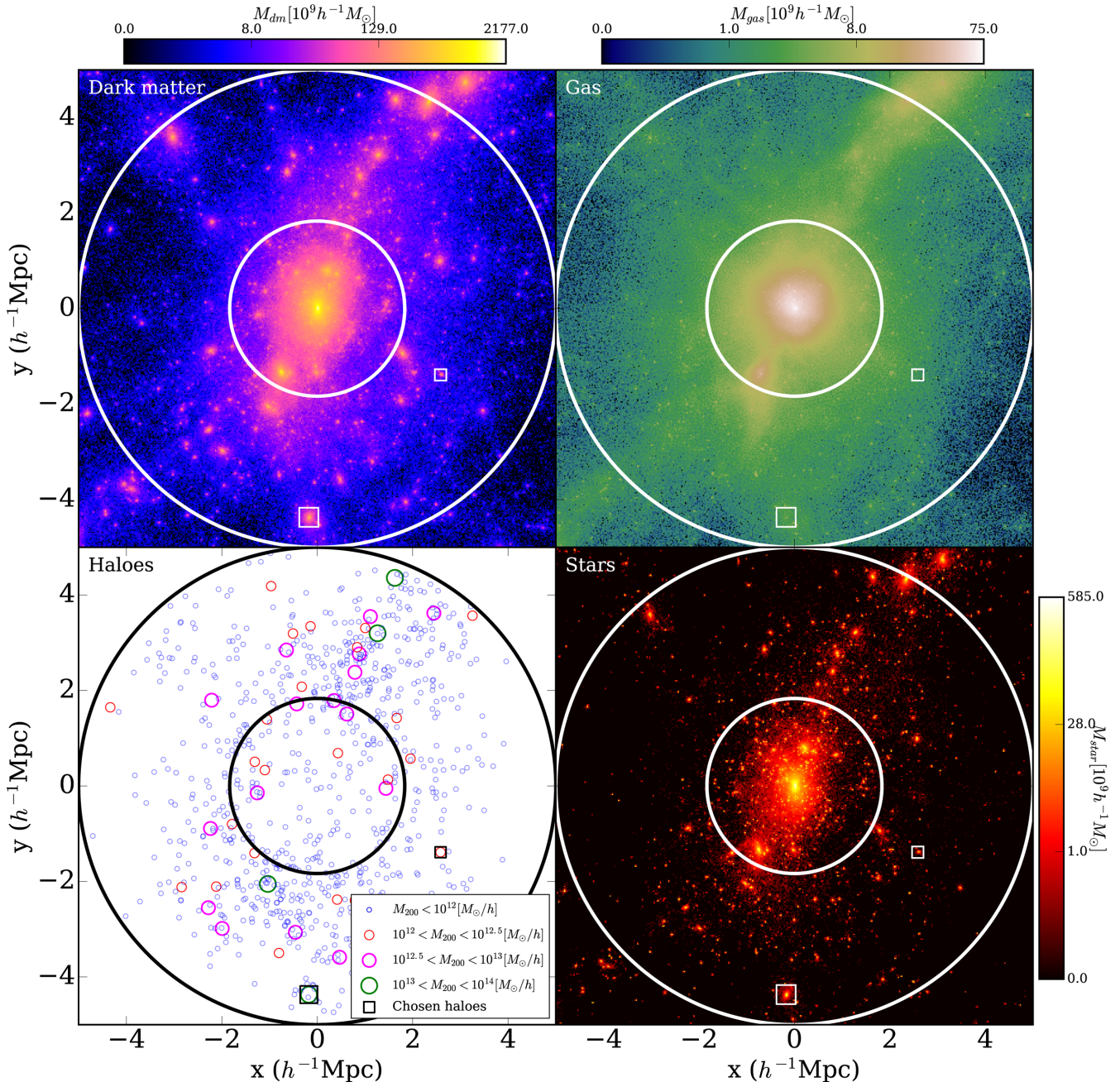


Figure 1. The distribution of DM (top left-hand panel), gas (top right-hand panel), stars (bottom right-hand panel) and haloes (bottom left-hand panel) for the G3-OWLS FP simulation. The colour bars are on a log scale. Each panel is $10 h^{-1}$ Mpc across. A circle of radius $5 h^{-1}$ Mpc is shown as a bold line on each panel. The inner circle indicates R_{200} for the G3-MUSIC simulation, which is used to delineate the central cluster region from the infall region that lies between the two circles. The circles marked on the bottom left-hand panel indicate the location of haloes or sub-haloes and are colour coded by mass as indicated in the legend. The black squares highlight the isolated haloes used for analysis in Fig. 7. These chosen haloes are also indicated on the other three panels with small white squares.

using this approach, so even if we included them in any further analysis we do not expect them to cause any significant statistical changes.

3 RESULTS

3.1 Haloes and galaxies

We begin our analysis by first presenting the cluster produced by G3-OWLS in Fig. 1. The top-left, top-right and bottom-right panels

show the projected density of DM, gas and stars across a $10 h^{-1}$ Mpc square centred on the cluster, respectively. Henceforth, we define the ‘central’ region of the cluster as the spherical volume contained within the inner circle, which is R_{200} ($1.8 h^{-1}$ Mpc) of the central halo in the G3-MUSIC reference simulation. The difference in R_{200} between the DM, NR and FP runs is $\lesssim 2$ per cent (Cui et al. 2016). We also define the ‘infall’ region as the shell between the inner and outer circles, where the latter defines the (somewhat arbitrary) $5 h^{-1}$ Mpc ($\sim 3R_{200}$) boundary in this paper. The last panel shows the haloes existing only in the infall region (the haloes in the central

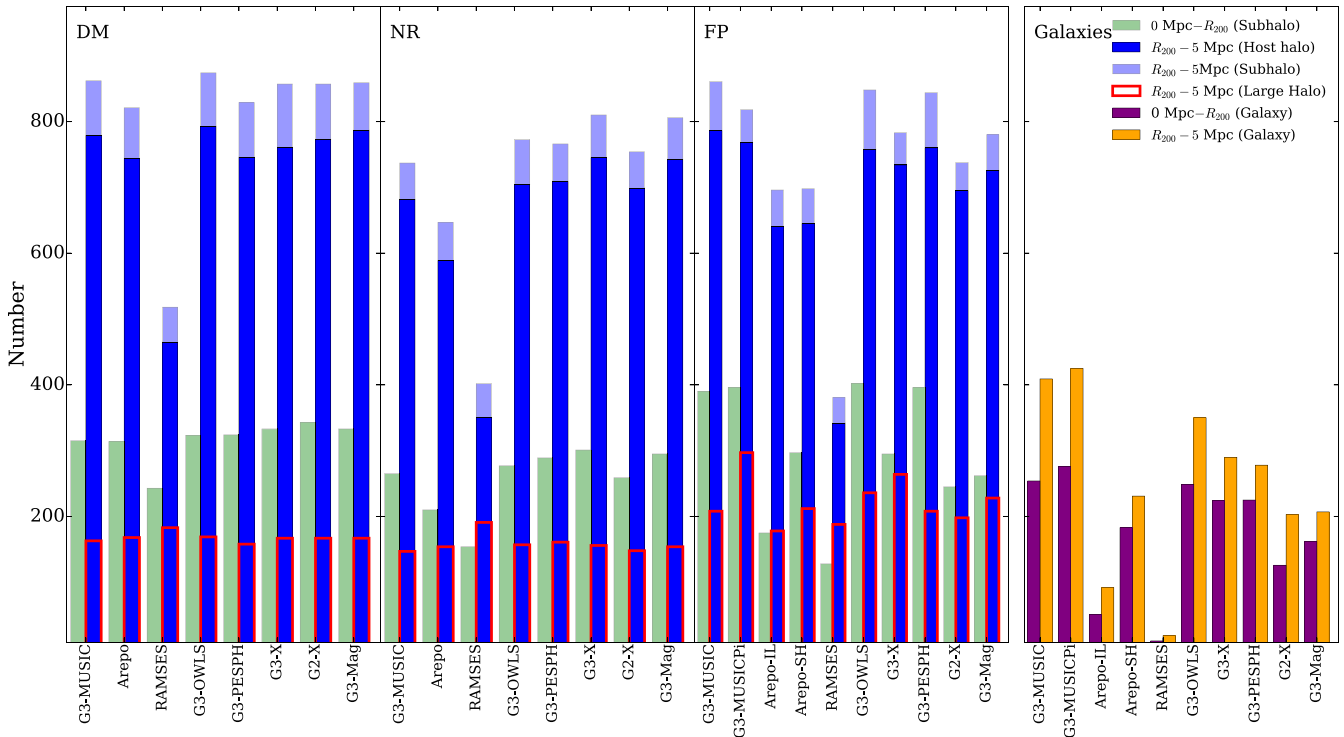


Figure 2. Number of haloes, sub-haloes and galaxies. The left, left-centre and right-centre panels show the number of haloes and sub-haloes for the DM-only, NR and FP runs, respectively. The right-hand panel shows the number of galaxies produced by each code in the FP run. In the first three panels, the green and blue bars represent different regions. The green bars are for the central virialized region inside R_{200} of the reference *G3-MUSIC* simulation. The blue bars are the infall region, between R_{200} and $5 h^{-1}$ Mpc. Solid bars represent haloes, whilst transparent bars stacked on top represent sub-haloes. The red outline indicates the number of large haloes, containing 200 or more particles. In the last panel, the purple and orange bars represent galaxies in the central and infall regions, respectively. For all simulations, there are ~ 10 times more haloes than sub-haloes in the infall region (blue), whilst in the central region (green) all but one of the objects are sub-haloes.

region are not plotted here). Any haloes residing within the central region in Fig. 1 are foreground objects.

There is clear filamentary structure surrounding the cluster at $z = 0$, with two particularly dense filaments running towards the bottom-left and top-right regions of each panel. In order to see how the most massive group-sized haloes are distributed in the infall region, we have partitioned the haloes into four mass bins, shown as different sizes and colours. After a 3D inspection, we find that ~ 60 per cent of haloes with mass $\sim 10^{12.5} - 10^{14} h^{-1} M_{\odot}$ reside within filamentary structure at $z = 0$, including 2–3 group-sized ($\gtrsim 10^{13} h^{-1} M_{\odot}$) haloes.

Our first code-to-code comparison in this study is presented in Fig. 2, where we show the number of haloes, sub-haloes and galaxies produced by each participating code. *AREPO-SH* and *G3-MUSICpi* only differ from their original variants in the FP run due to their variant sub-grid prescriptions, so no values are shown for these codes in the DM-only and NR runs.

Fig. 2 shows that nearly all codes produce a consistent number of haloes and sub-haloes in both the infall and central regions in all runs, though there is more code-to-code scatter in the NR and FP runs due to the inclusion of uncertain baryonic physics. The exception is *RAMSES*, which produces nearly a factor of 2 fewer objects than the median in the infall region across all runs. However, when we consider the large haloes in the infall region that have a minimum of 200 DM particles (red-edged bars), we see that the codes are more consistent with each other across all runs, even *RAMSES*. This suggests that *RAMSES* is not resolving haloes that contain less than ~ 200 particles, which has been shown before in AMR codes

(O’Shea et al. 2005). In this instance, *RAMSES* probably just needs to use a mesh with better resolution in order to resolve the smaller objects.

All codes produce ~ 10 times more haloes (solid blue bars) than sub-haloes (transparent blue bars stacked on top) in the infall region across all runs, whilst nearly all objects in the central region are sub-haloes residing within R_{200} of the main cluster halo. The lack of sub-haloes in the infall region indicates that in this cluster at $z = 0$ our halo sample is not heavily contaminated by sub-haloes currently undergoing some pre-processing. DM-only simulations produce similar sub-halo to halo ratios, for example Klypin, Trujillo-Gomez & Primack (2011) showed that in the Bolshoi simulation the ratio between sub-halo and halo abundances is typically ~ 10 –20 per cent for halo masses between $\sim 10^9$ and $10^{14} h^{-1} M_{\odot}$. The low number of sub-haloes that surround the cluster at $z = 0$ may at first appear in tension with recent observational studies that have suggested pre-processing is a dominant mechanism at $z \sim 0$ (Cybulski et al. 2014; Just et al. 2015). However, we should note that this may not be a fair comparison and we intend to carry out a full temporal study to investigate pre-processing as this cluster forms in future work.

E16 showed that there was a large inconsistency between codes in how many galaxies they produced within the central $2 h^{-1}$ Mpc region; the scatter between codes extended up to a factor of ~ 20 . Whilst Fig. 2 corroborates this, the most notable result is that this code-to-code scatter persists out to the infall region as well, suggesting that it may not be the different gas environments driving the code-to-code scatter, but the different sub-grid schemes each code

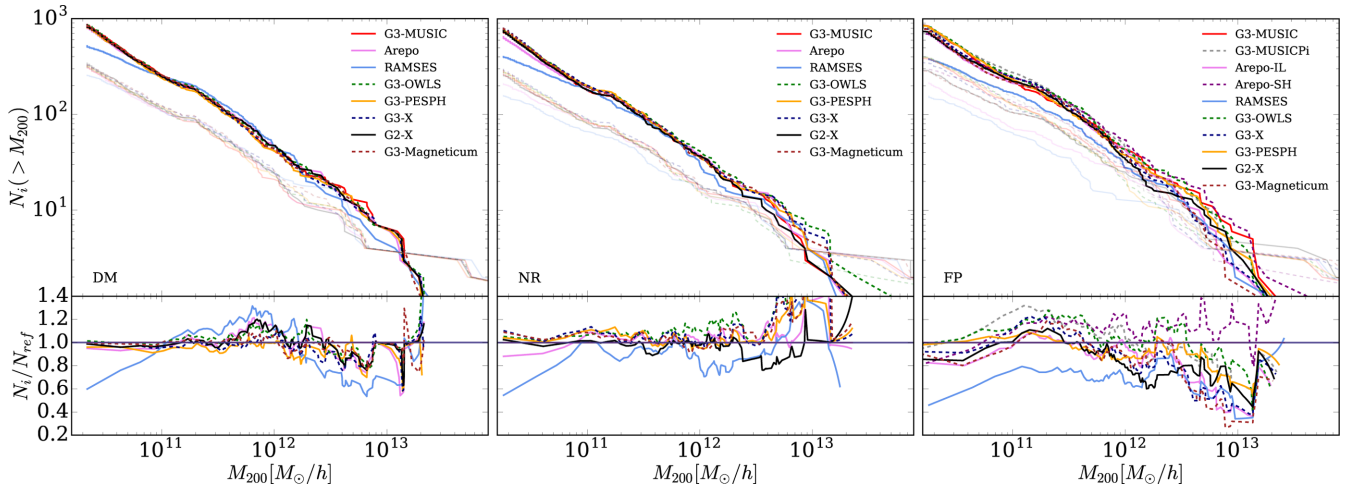


Figure 3. The top panels show the cumulative halo (including sub-halo) mass functions for each simulation only considering the DM component of the objects, while the bottom panels show the ratio between each simulation and the reference model, G3-MUSIC. The left-, centre and right-hand panels show the results from the DM-only, NR and FP runs, respectively. Transparent and opaque lines represent the central and infall regions, respectively. The transparent lines have only been included to show how the code-to-code scatter in the central region compares to the infall region; see Elahi et al. (2016) for detail about the central region. The infall region contains more than twice as many haloes as the central region. RAMSES is an outlier even for the DM-only run in the infall region, with many small haloes missing. These missing haloes extend to around $10^{12} h^{-1} M_{\odot}$ (over 1000 particles) in the FP run where the total number of haloes present in the infall region is around 40 per cent of that seen in the other models.

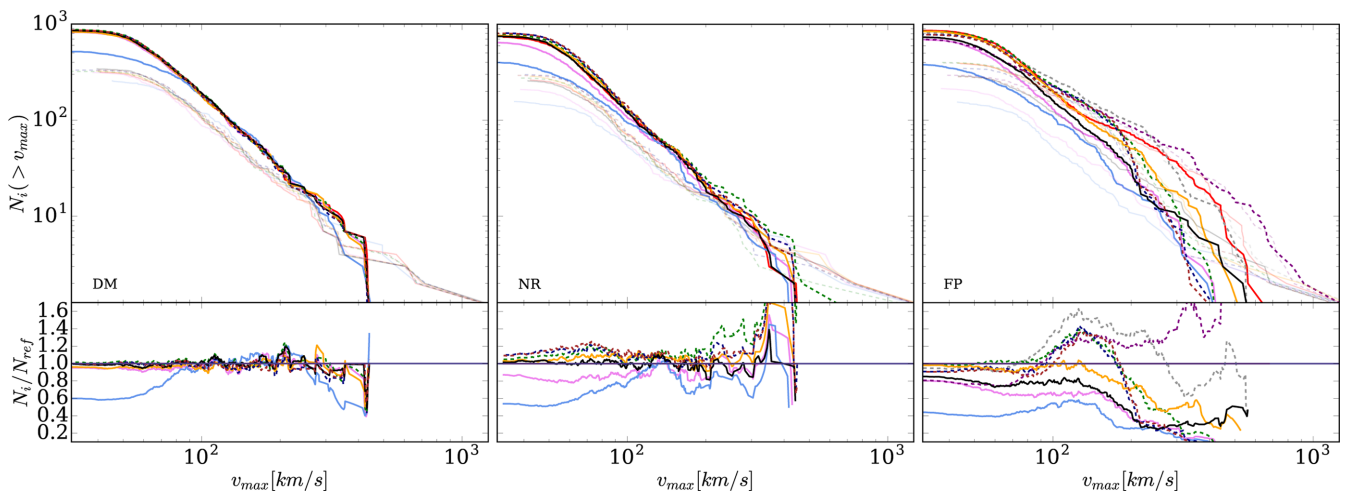


Figure 4. Similar to Fig. 3, but for the cumulative maximum circular velocity distribution (see Fig. 3 for legend). The plots show similar results to Fig. 3, though here in the FP run the code-to-code scatter is amplified compared to the corresponding cumulative mass function.

employs. In the infall region, G3-MUSIC and G3-MUSICPI produce the most galaxies, which is expected as these two codes do not include AGN feedback and only moderate gas cooling with stellar feedback. AREPO-IL and RAMSES produce a factor of ~ 3 and ~ 13 fewer galaxies than the median, respectively, a potential consequence of powerful AGN feedback tuned to match the properties of the central halo, which is quenching smaller objects very efficiently. We are confident that the scatter in galaxy abundances between codes here is not due to poorly resolved galaxies, as we see the code-to-code scatter extends up to a factor of $\gtrsim 25$ for well-resolved galaxies as well ($M_{200} \gtrsim 10^{10} h^{-1} M_{\odot}$) as seen later in the text.

We next investigate the mass functions and circular velocity distributions of haloes and sub-haloes, shown in Figs 3 and 4, respectively. A value for M_{200} can be calculated for sub-haloes in a similar fashion to haloes; however, when R_{200} cannot be found, M_{200} is set to equal the total mass of the sub-halo. We have displayed these distributions for both the central (transparent) and

infall (opaque) regions. The mass functions for the central region have only been included to show how the code-to-code scatter in the central region compares to the infall region; see E16 for more detail about the central region. The lower panels in these figures show the residuals of these distributions in the infall region relative to the G3-MUSIC reference simulation. In the infall region, the codes produce a largely consistent set of mass functions (Fig. 3, solid lines) in the DM-only run, where the typical scatter is $\lesssim 10$ per cent. As found in E16, we note that this scatter is increased in the NR run to $\lesssim 15$ per cent, because of the inclusion of gas and the different hydrodynamic approaches each code uses to evolve the gas particles. The code-to-code scatter is then amplified in the FP run to typically ~ 60 per cent for all haloes, with the addition of uncertain sub-grid effects. All codes produce twice as many haloes and sub-haloes with mass $\lesssim 10^{12} h^{-1} M_{\odot}$ in the infall region compared to the centre across all runs. In total, there are ~ 3 times as many haloes and sub-haloes in the infall region (~ 900 objects) compared to the centre

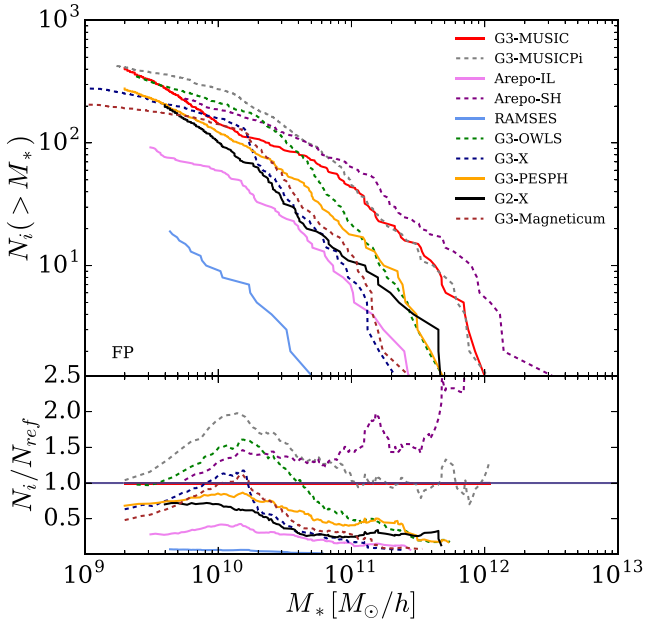


Figure 5. The top panel shows the cumulative galaxy stellar mass distribution in the cluster infall region, whilst the bottom panel shows the ratio of each code relative to the G3-MUSIC simulation. Even above $10^{11} h^{-1} M_{\odot}$, the code-to-code scatter extends beyond ~ 100 per cent.

(~ 300 objects), which allows us to utilize a statistically robust sample of objects for this study.

In the DM-only run, RAMSES produces ~ 40 per cent fewer haloes and sub-haloes with mass $\lesssim 10^{11} h^{-1} M_{\odot}$ compared to all other codes in the infall region, a number which is consistent with Fig. 2. This is amplified in the FP run, where RAMSES produces ~ 50 per cent fewer haloes with mass $\lesssim 10^{12} h^{-1} M_{\odot}$ compared to most other codes. It is clear that the combination of absent low-mass haloes and powerful AGN feedback has a dramatic effect on even quite large haloes for RAMSES, impacting their number even for haloes that contain several thousand particles.

As the recovered mass (in this case M_{200}) is not observable, in Fig. 4 we present the maximum circular velocity distributions. As Knebe et al. (2011) demonstrated, these are less susceptible to outer boundary issues but require more particles to measure reliably and are known to be sensitive to central concentrations of sub-haloes (Onions et al. 2013). In Fig. 4, nearly all codes are in good agreement in the DM-only and NR runs, but the underproduction of low-mass haloes by RAMSES and to some extent AREPO in the NR run is even more apparent. The most notable change in the maximum circular velocity distributions is the significant increase in code-to-code scatter in the FP run compared to the corresponding mass function. Typically the scatter in the FP mass function is ~ 60 per cent, whilst in the FP circular velocity distribution the code-to-code scatter extends up to ~ 100 – 150 per cent. Clearly, the additional physics contained in the FP runs influences the central regions which are being probed by the measurement of the maximum circular velocity and this could be problematic for this approach. Interestingly, we find that the code-to-code scatter in the FP circular velocity distribution reaches a factor of more than 2 at $v_{\max} \sim 200 \text{ km s}^{-1}$, which corresponds to a halo mass $\sim 5 \times 10^{12} h^{-1} M_{\odot}$. It is clear that this scatter is not due to poorly resolved haloes but more likely the internal sub-grid prescriptions.

In Fig. 5, we present the cumulative Galaxy Stellar Mass Function (GSMF) of galaxies in the cluster infall region produced by

each code. The top panel shows the cumulative distribution, whilst the bottom panel shows the ratio of each GSMF with the GSMF produced by the G3-MUSIC reference simulation. The most notable result shows that above $10^{10} h^{-1} M_{\odot}$, where the galaxies are well resolved (these galaxies will contain $\gtrsim 100$ star particles), the scatter between the codes is of order ~ 100 per cent.

The inability of RAMSES to resolve small haloes coupled with the fact that it employs a powerful AGN feedback scheme causes the code to produce no galaxies above $\sim 10^{10.6} h^{-1} M_{\odot}$, and below this mass RAMSES produces an order of magnitude fewer galaxies compared to the other codes. Conversely, AREPO-SH produces the most massive galaxies primarily because it does not include an AGN feedback scheme.

3.2 Baryonic content

In order to further investigate what impact the different sub-grid prescriptions have on the cluster centre and infall regions, we next study the baryonic material contained within the haloes. In Fig. 6, we show the gas fraction versus stellar fraction of all haloes and sub-haloes contained within the entire $5 h^{-1} \text{ Mpc}$ region. We have split these haloes into four different mass (M_{200}) bins, shown as different panels in the figure. Observational constraints have also been plotted in each mass bin. The cosmic baryon fraction from WMAP7 data in Komatsu et al. (2011) is plotted as a dark-grey curve.

Observed stellar fractions in each mass bin from halo abundance matching relations in Behroozi et al. (2013) and Kravtsov et al. (2014) are shown as green and blue patches, respectively. The limits of the patches show the minimum and maximum points in stellar fraction from these trends in each mass range and are therefore largely exaggerated. Each halo abundance matching trend is derived from a different set of stellar mass functions, which causes some discrepancy between the two, especially in the largest mass bin. The reason why this discrepancy is so large in the largest halo bin is that the stellar mass function (Bernardi et al. 2013) used in Kravtsov et al. (2014) employs an improved photometric method that accounts for the extended stellar envelope surrounding the central BCG. This would lead one to assume that the Kravtsov et al. (2014) relation is better suited for modelling galaxy clusters.

This raises the important point that when models calibrate their stellar fraction in the main halo to observational data, they should not include all stellar material contained within the halo as the observations do not account for this. For instance, in this paper we calculate stellar fractions within a sphere of radius $30 h^{-1} \text{ kpc}$ centred on the centre of mass of each halo. For all haloes except the main cluster halo, the differences in simulated stellar fractions between the $30 h^{-1} \text{ kpc}$ or whole halo apertures is low ($\lesssim 5$ per cent). However, for the main halo we find that ~ 80 per cent of stars are located outside the $30 h^{-1} \text{ kpc}$ aperture and are part of the intracluster light. Some fraction of stars contained within the intracluster light is partly a numerical artefact associated with simulations at this resolution, and how to deal with them when comparing to observations is still a matter of debate which will be explored in more detail in (Cui et al., in preparation). For this study, we note that using different sensible apertures does not affect the stellar fractions dramatically; for instance, changing our $30 h^{-1} \text{ kpc}$ aperture to $50 h^{-1} \text{ kpc}$ equates to a change in stellar fraction of only $\lesssim 10$ per cent. In this study, we are not worried about this discrepancy as we are not comparing the codes to strict observational limits, as even the two trends included in this paper are in tension in certain mass bins.

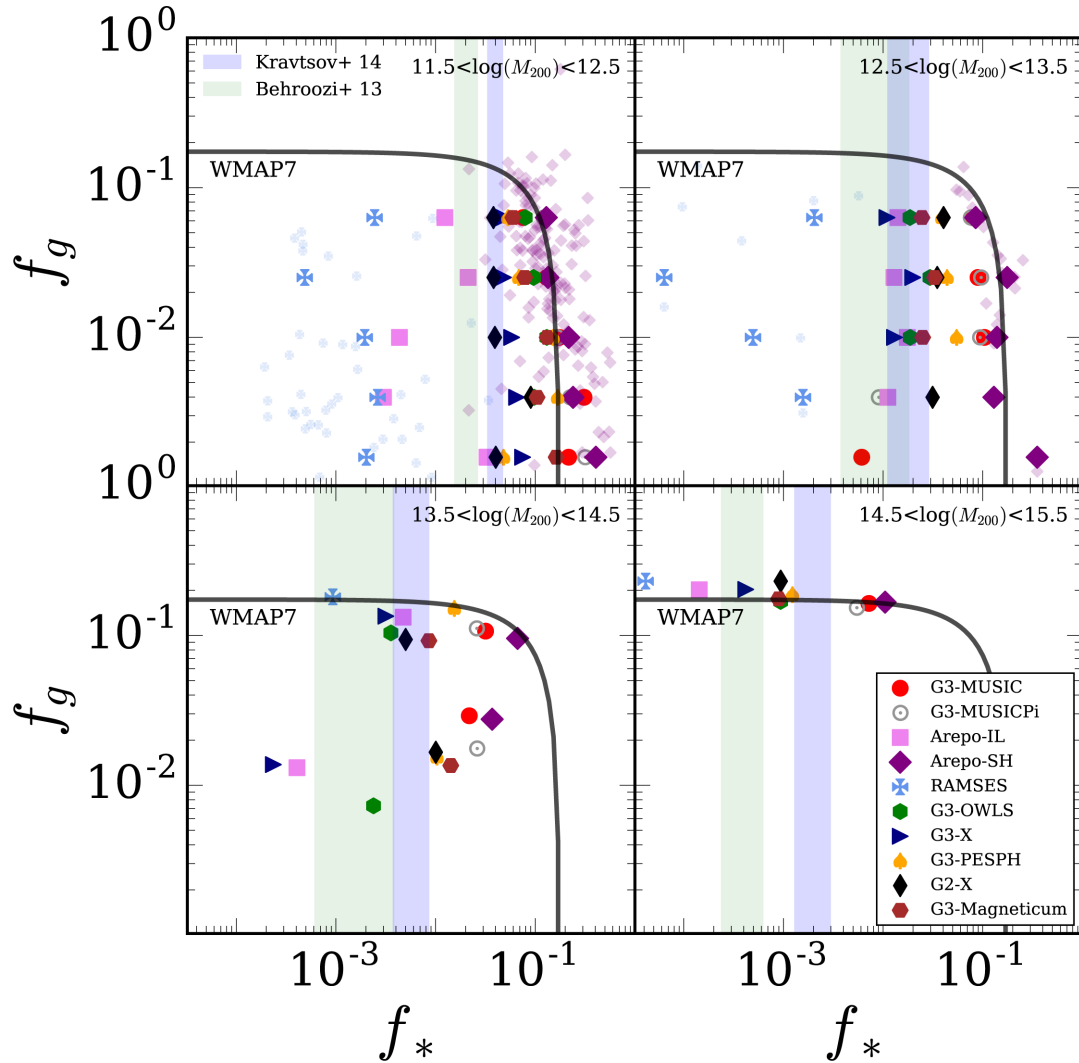


Figure 6. Gas fraction versus stellar fraction in four different halo mass (M_{200}) bins as indicated in each panel. The highest mass bin, bottom right, shows the baryonic content contained within the main central halo. The bottom left-hand panel indicates the baryonic content for the two most massive sub-halos in the main halo. In the top panels, the large markers represent the average stellar fraction in five gas fraction bins, whilst the small markers show the true distribution for the two most extreme cases, RAMSES and AREPO-SH. The cosmic baryon fraction (Ω_b/Ω_m) is shown in each panel as a solid grey curve. The green and blue shaded regions represent observational constraints from Behroozi, Wechsler & Conroy (2013) and Kravtsov, Vikhlinin & Meshcheryakov (2014), respectively. The limits of each observational patch are simply the allowed upper and lower limit in stellar fraction in each mass bin found from each trend. For each code, the haloes tend to lie in vertical bands of stellar fraction and this rank ordering is roughly preserved with mass.

The bottom right-hand panel is the equivalent to fig. 1 in Paper II, showing the baryon fraction for the central cluster halo but considering baryonic material within M_{200} instead of M_{500} . It is clear from this panel that several codes do not reproduce observed stellar fractions. G3-MUSIC, G3-MUSICPi and AREPO-SH create too many stars by nearly one order of magnitude in the centre compared to observations, which again is not surprising as these codes do not contain AGN feedback. As mentioned before, it is difficult to suggest robust allowed regions of stellar fractions, as even the observations are discrepant by 0.5 dex in this mass bin, but the codes should ideally be aiming to be broadly consistent with at least one set of observations. RAMSES drastically underproduces stars compared to the observations by ~ 1 order of magnitude. For this single halo, G3-MAGNETICUM, G3-PESPH, G3-OWLS, G2-X and G3-X produce stellar fractions that lie between the observations. The bottom left-hand panel indicates where the next two largest haloes lie on this plane. As already discussed, these are both within R_{200} and so they are

sub-haloes of the main halo. The code-to-code scatter extends above 2 dex here in stellar fraction.

Interestingly, the ordering of the codes in stellar fraction seen in the bottom panels remains at lower masses where the objects are largely haloes in the infall region. Here the large symbols show the average stellar fraction in each gas fraction bin, whilst the small transparent symbols show the scatter for the two most extreme codes, RAMSES and AREPO-SH. Averaged over many haloes, G3-OWLS, G3-X, G3-MAGNETICUM and AREPO-IL produce stellar fractions that are more consistent with observations at lower halo masses. Again, RAMSES does not create enough stars by $\sim 1-2$ orders of magnitude. At these masses, we expect the inability of RAMSES to resolve low-mass haloes to seriously inhibit its ability to reproduce observed stellar fractions. Again, the stellar fractions for the two G3-MUSIC variants and AREPO-SH are too high, deliberately in the case of AREPO-SH as this simulation was included to demonstrate the difference turning off AGN feedback made.

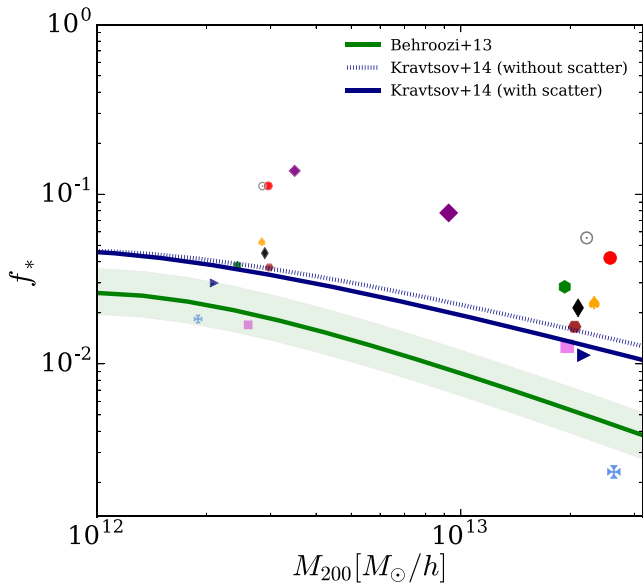


Figure 7. A one-to-one comparison of stellar fraction versus halo mass for the two isolated haloes marked in Fig. 1 that are common to all the simulations. The smaller and larger markers correspond to a $\sim 10^{12}$ and $\sim 10^{13} h^{-1} M_{\odot}$ mass halo, respectively, which are both shown as black squares in the bottom right-hand panel of Fig. 1. Observational constraints from Behroozi et al. (2013) and Kravtsov et al. (2014) are also shown as indicated by the legend. Even for both of these relatively isolated haloes, the code-to-code scatter is still above an order of magnitude.

The conservation of code ordering in stellar fraction between all four panels again suggests that the primary driver of the scatter is the various sub-grid physics implementations, rather than any environmental differences in gas between the codes. We investigated this further by studying the stellar fraction of two specific matched haloes in the infall region, marked as black squares in the bottom left-hand panel of Fig. 1. We chose these two haloes because they were common to all simulations and because they are relatively isolated, so we expect the local gas environments to be more consistent between the models. In this case, isolation means that the haloes are well separated from any comparable or larger halo. For instance, the two haloes have masses $\sim 10^{12}$ and $\sim 10^{13} h^{-1} M_{\odot}$, and the distance from these objects to any other objects with the same mass or above is ~ 2.4 and $\sim 3.2 h^{-1} \text{Mpc}$, respectively. The haloes were matched between models by using their halo position and mass.

Fig. 7 shows the stellar fraction versus M_{200} for the isolated haloes that are produced by each code, along with the observational constraints from Behroozi et al. (2013) and Kravtsov et al. (2014). The green shaded regions associated with the Behroozi et al. (2013) trend are the 1σ errors obtained from their Markov chain Monte Carlo (MCMC) analysis. Two trends are displayed from Kravtsov et al. (2014), one with and one without scatter, where the latter includes artificial scatter when the haloes are populated with galaxies in the abundance matching technique. For both haloes, the code ordering in stellar fraction is again preserved (with small discrepancies) and the code-to-code scatter is still significant. For instance, for the $\sim 10^{12} h^{-1} M_{\odot}$ halo the difference between the most outlying codes is 0.85 dex, whilst for the $\sim 10^{13} h^{-1} M_{\odot}$ halo it is 0.7 dex, when not including RAMSES. Because this amount of scatter is still present in the isolated haloes, we conclude that the differences in the internal sub-grid schemes are driving a large proportion of the code-to-code scatter rather than the different gas environments between the codes.

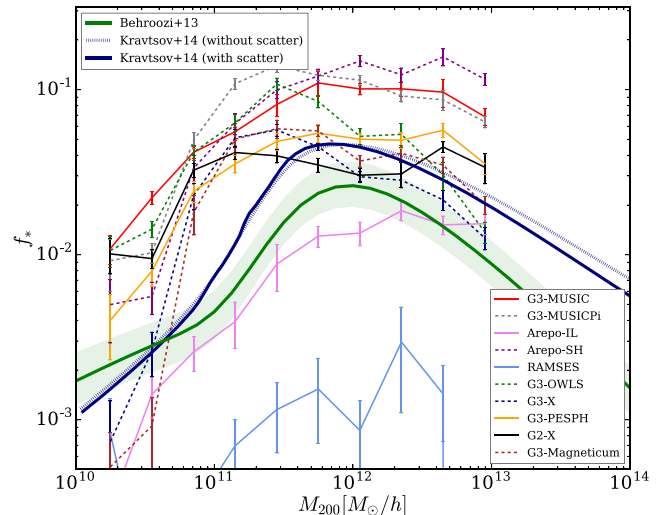


Figure 8. Stellar fraction versus halo mass for each code in the cluster infall region. The average stellar fractions in each M_{200} bin are presented along with 1σ errors from the mean obtained from bootstrap sampling. Again, observational constraints from Behroozi et al. (2013) and Kravtsov et al. (2014) are also shown as indicated by the legend. At low masses, nearly all the codes overproduce stars. Five codes produce infall haloes that contain stellar fractions that are more consistent with observations above $\sim 10^{12} h^{-1} M_{\odot}$. RAMSES underproduces stars at all halo masses.

We have further investigated the stellar fraction versus M_{200} relation for all haloes in the infall region in Fig. 8. Average stellar fractions in M_{200} mass bins are presented for each code along with 1σ error bars from the mean obtained from bootstrap sampling. Apart from AREPO-IL and RAMSES, all codes overproduce stars by ~ 0.1 – 0.6 dex below $M_{200} \sim 10^{11.25} h^{-1} M_{\odot}$. G3-OWLS, G3-MAGNETICUM, G2-X, G3-X and AREPO-IL produce stellar fractions that are more consistent with either set of observations above $M_{200} \sim 10^{12} h^{-1} M_{\odot}$. RAMSES does not produce enough stars by an order of magnitude compared to the Behroozi et al. (2013) trend across all mass ranges. This figure is troubling, as in cluster simulations it is imperative that all codes are able to match observed stellar fraction versus M_{200} relations, especially in the infall region as these haloes will eventually go on to build the central halo. This issue is becoming increasingly important as galaxy cluster simulations are now being used more widely for cluster cosmology validation (e.g. McCarthy et al. 2016) and environmental galaxy quenching studies (e.g. Bahé & McCarthy 2015).

We end our analysis with Fig. 9 where we investigate the fraction of gas-poor ($f_g < 10^{-2}$) haloes at $z = 0$ in each code as a function of halo mass in the infall (solid lines) and central (dashed lines) regions. This allows us to investigate the differences in gas environments between each code in both regions and to find out which mechanisms may be driving gas out of the haloes. We have done this for both the NR and FP runs, shown in the top and bottom panels, respectively.

The NR run contains a higher fraction of gas-poor haloes compared to the FP run. Above $\sim 10^{11} h^{-1} M_{\odot}$ where haloes are more resolved (haloes below this mass contain < 100 particles), the codes in the NR run produce gas-poor fractions that are typically ~ 50 per cent larger than their FP counterparts. However, with the inclusion of star formation and feedback processes in the FP run, we would naively expect there to be a higher gas-poor fraction here. Presumably, this means that either the extra gravitational pull from the stars is enough to retain the gas or that the employed feedback schemes are not powerful enough to drive outflows, which could

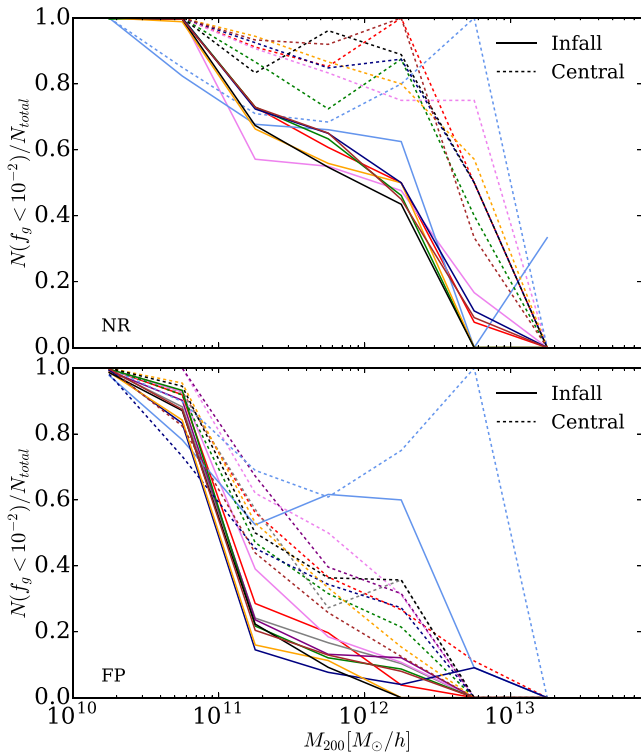


Figure 9. The fraction of gas-poor ($f_g < 10^{-2}$) haloes as a function halo mass. The NR and FP simulations are shown in the top and bottom panels, respectively. Solid lines represent haloes in the infall region, whilst dashed lines show haloes in the central region. See legend in Fig. 3 for which coloured line corresponds to which code. In both the central and infall regions, codes produce gas-poor fractions that are typically ~ 50 per cent higher in the NR run compared to the FP run. Codes also tend to produce ~ 20 – 30 per cent higher gas-poor fractions in the central region compared to the infall region in both the NR and FP runs.

be linked to the overcooling problems seen in Fig. 6. However, the reason for the discrepancy between the NR and FP runs could be that the gas in the NR run cannot cool, unlike in the FP run. Therefore, the gas may remain extended in the NR run and more easily stripped.

There are also differences in the gas-poor fractions between the central and infall regions. In both the NR and FP run, codes in the central region typically produce gas-poor fractions that are ~ 20 – 30 per cent larger than the infall region. We expect the differences in the gas-poor fractions between the central and infall regions to be predominantly due to the gas in the haloes being more efficiently stripped in the centre by the increased ram pressure.

4 DISCUSSION AND CONCLUSIONS

Hydrodynamical simulations of galaxy clusters are now vital tools for interpreting and understanding observational data. However, it is vital that the validity of the models used to produce such simulations is checked by carrying out model comparison studies. This paper is a continuation of one such study, the *nIFTy cluster comparison project* whose aim is to take eight state-of-the-art hydrodynamical codes each equipped with its own calibrated sub-grid physics and to examine a $M_{200} = 1.1 \times 10^{15} h^{-1} M_{\odot}$ galaxy cluster each model produces from the same initial conditions.

In this paper, we have studied the properties of haloes, sub-haloes and galaxies residing in the infall region ($R_{200} = 5 h^{-1} \text{Mpc}$

($\sim 3R_{200}$) surrounding this cluster. This is an extension of the work done in E16 who carried out a similar study inside R_{200} of the same synthetic cluster, where they found striking code-to-code differences in galaxy abundances and mass.

We have studied how well each model reproduces observed stellar fraction versus halo mass relations, further investigated the sources of code-to-code scatter seen in E16 and examined the extent to which ongoing pre-processing is occurring in the infall region at $z = 0$. Our main conclusions are presented below along with some discussion.

(i) We have presented the $M_{200} = 1.1 \times 10^{15} h^{-1} M_{\odot}$ nIFTy galaxy cluster showing the DM, gas and stellar content along with the halo distribution in the infall region. It is clear that the galaxy cluster is surrounded by obvious filamentary structure that hosts 2–3 group-sized ($> 10^{13} h^{-1} M_{\odot}$) haloes.

(ii) After comparing the number of haloes and sub-haloes between codes in the infall region, we have found that although there is more scatter in the FP run compared to the DM-only and NR runs, the code-to-code scatter is still < 15 per cent. The exception is the AMR code RAMSES, which produces a factor of 2 fewer haloes and sub-haloes than the median. Along with an overpowered AGN feedback scheme, this is partly a resolution issue that is inherent to AMR codes as RAMSES is more aligned with other codes for haloes containing 200 DM particles or more.

(iii) The code-to-code scatter in galaxy abundance in the central region seen in E16 extended up to a factor of ~ 20 between the two most extreme cases. We have shown that the same degree of scatter is still present in the infall region as well, which suggests that the code-to-code scatter seen in E16 is predominantly due to the different sub-grid implementations employed by each code, rather than any differences in gas environments between the codes, which would be exacerbated in the overdense central region compared to the infall region. Codes without AGN feedback such as G3-MUSIC, G3-MUSICPI and AREPO-SH produce the most galaxies, whilst RAMSES and AREPO-IL produce the least.

(iv) In all codes we have shown that there are ~ 10 times more haloes than sub-haloes in the infall region, which is as expected from DM-only simulations (e.g. Klypin et al. 2011). The small sub-halo to halo ratio suggests that there may not be much ongoing pre-processing at $z = 0$, which would be in tension with recent observational studies that have suggested pre-processing is a dominant mechanism in the infall region at $z \sim 0$ (Cybulski et al. 2014; Just et al. 2015). However, we caution that this may not be a fair comparison, and we intend to carry out a full temporal study in order to investigate pre-processing in the infall region as this cluster forms.

(v) We also compared estimates of halo mass and maximum circular velocity, which has been suggested as a better statistic from which to derive mass. We notice a significant increase in code-to-code scatter in the measurement of the maximum circular velocity for large haloes in the FP models compared to the M_{200} estimate. This is because the maximum circular velocity occurs close to the halo centre and this region is significantly disturbed by the feedback schemes employed in the FP run. We caution that the use of maximum circular velocity may not lead to the significant improvement suggested for FP models.

(vi) We have shown that five codes do not reproduce observed stellar fractions (Behroozi et al. 2013; Kravtsov et al. 2014) for the main cluster halo, typically the ones not containing AGN feedback that overproduce stars, as well as AREPO-IL and RAMSES, which underproduce stars compared to observations. For this halo, the scatter in stellar fraction between the two most extreme codes is around two

orders of magnitude. Averaged over many haloes, the story is the same at lower halo masses, where the same degree of code-to-code scatter is still present and the rank ordering of codes in stellar fraction is roughly preserved. G3-X and G3-OWLS are the most consistent with observations in all mass bins in Fig. 6. However, we do caution that the two observational trends used in this study are in tension with each other, due to the different set stellar mass functions each uses to produce its relations. Though we expect the Kravtsov et al. (2014) relation to be more suitable at the high-mass end due to its use of a stellar mass function (Bernardi et al. 2013), which uses an improved photometric method to capture the outer envelope of the cluster BCG.

(vii) After analysing the stellar fractions of two isolated haloes (with mass $\sim 10^{12}$ and $\sim 10^{13} h^{-1} M_{\odot}$) common to all models in the infall region, we find that the code-to-code scatter is still above >1 dex for both objects. As these haloes are far enough away from any neighbouring haloes of comparable mass ($>2 h^{-1}$ Mpc), we expect this scatter to be predominantly due to the differences in the internal sub-grid implementations rather than any external gas environment differences between the models.

(viii) By comparing the stellar fraction versus M_{200} of all haloes only in the infall region to observed trends from Behroozi et al. (2013) and Kravtsov et al. (2014), we find that G3-OWLS, G3-MAGNETICUM, G2-X, G3-PESPH, G3-X and AREPO-IL are reasonably consistent with either set of observations above $\sim 10^{11.25} h^{-1} M_{\odot}$ (differences between models and observations here are typically $\lesssim 0.2$ dex). Below this mass, all of the GADGET variant models produce too many stars compared to the observed stellar fractions by nearly an order of magnitude, which is presumably a resolution issue as these haloes will only contain $\lesssim 100$ particles. This issue is hard to solve as it is often unfeasible to produce massive galaxy cluster simulations with better resolution than in our study. G3-MUSIC, G3-MUSICPI, AREPO-SH and RAMSES are discrepant with observations at all halo masses by $\gtrsim 0.5$ dex, because they either do not contain AGN feedback (deliberately in the case of AREPO-SH) or in the RAMSES case the AGN is far too powerful.

(ix) The inability of RAMSES to reproduce observations by consistently underproducing stellar material within haloes and sub-haloes of every mass is in stark tension with the Rhapsody-G simulations studied in Hahn et al. (2015). They studied 10 galaxy clusters simulated with RAMSES of similar mass and resolution to the nIFTy cluster and found good agreement between the stellar content contained within the haloes and sub-haloes surrounding the clusters and halo abundance matching trends. We suspect the differences between these two results to arise from the fact that RAMSES includes variant sub-grid prescriptions between the two runs that have been calibrated differently. Many sub-grid models can be calibrated to reproduce different targeted observables, but this does not necessarily mean one is more accurate or reliable than the other. These sub-grid models are simply recipes with knobs that can be turned in order to reproduce specific things, and one cannot disregard one code because it does not match one key observable.

In the future, we expect these codes and many more to continuously improve by incorporating more realistic sub-grid models that are extensively calibrated to current and new observables (e.g. McCarthy et al. 2016) at $z = 0$ and above, which in turn will lead to more accurate cluster simulations from which valuable science can be done. We next intend to carry out a full temporal study within a larger $25 h^{-1}$ Mpc zoom region surrounding this cluster in order to investigate the assembly history of the cluster and the effectiveness of pre-processing at higher redshift.

ACKNOWLEDGEMENTS

The authors would like to acknowledge the Centre for High Performance Computing in Rosebank, Cape Town, for financial support and for hosting the ‘Comparison Cape Town’ workshop in 2016, July. The authors would further like to acknowledge the support of the International Centre for Radio Astronomy Research (ICRAR) node at the University of Western Australia (UWA) in hosting the precursor workshop ‘Perth Simulated Cluster Comparison’ in 2015, March; the financial support of the UWA Research Collaboration Award 2014 and 2015 schemes; the financial support of the ARC Centre of Excellence for All Sky Astrophysics (CAASTRO) CE110001020 and ARC Discovery Projects DP130100117 and DP140100198. We would also like to thank the Instituto de Fisica Teorica (IFT-UAM/CSIC in Madrid) for its support, via the Centro de Excelencia Severo Ochoa Program under Grant No. SEV-2012-0249, during the three-week workshop ‘nIFTy Cosmology’ in 2014, where the foundation for the whole comparison project was established.

JA acknowledges support from a post-graduate award from STFC. PJE is supported by the SSIMPL programme and the Sydney Institute for Astronomy (SIfA) and Australian Research Council (ARC) grants DP130100117 and DP140100198. AK is supported by the Ministerio de Economía y Competitividad (MINECO) in Spain through grant AYA2012-31101 as well as the Consolidation-Ingenuo 2010 Programme of the Spanish Ministerio de Ciencia e Innovación (MICINN) under grant MultiDark CSD2009-00064. He also acknowledges support from the ARC grant DP140100198. He further thanks Noonday Underground for surface noise. STK acknowledges support from STFC through grant ST/L000768/1. CP acknowledges the support of the ARC through Future Fellowship FT130100041 and Discovery Project DP140100198. WC and CP acknowledge the support of ARC DP130100117. GY and FS acknowledge support from MINECO (Spain) through the grant AYA 2012-31101. GY thanks also the Red Española de Supercomputación for granting the computing time in the Marenostrum Supercomputer at BSC, where all the MUSIC simulations have been performed. AMB is supported by the DFG Research Unit 1254 ‘Magnetisation of interstellar and intergalactic media’ and by the DFG Cluster of Excellence ‘Universe’. GM acknowledge support from the PRIN-MIUR 2012 Grant ‘The Evolution of Cosmic Baryons’ funded by the Italian Minister of University and Research, by the PRIN-INAF 2012 Grant ‘Multi-scale Simulations of Cosmic Structures’, by the INFN INDARK Grant and by the ‘Consorzio per la Fisica di Trieste’. IGM acknowledges support from an STFC Advanced Fellowship. EP acknowledges support by the ERC grant ‘The Emergence of Structure During the Epoch of Reionization’.

The authors contributed to this paper in the following ways: JA, FRP, MEG, PJE and AK formed the core team. JA analysed the data, made the plots and wrote the paper. FRP and MEG assisted in writing the paper. PJE assisted with the analysis. AK, GY and FRP organized the nIFTy workshop. GY supplied the initial conditions. All other authors performed simulations using their codes or read and commented on the paper.

The simulations used for this paper have been run on a variety of supercomputers and are publicly available at the MUSIC website, <http://www.music.ft.uam.es>. MUSIC simulations were carried out on Marenostrum. AREPO simulations were performed with resources awarded through STFCs DiRAC initiative. The authors thank Volker Springel for helpful discussions and for making AREPO and the original GADGET version available for this project. The authors also thank Andrey Kravtsov for useful discussions. G3-PESPH simulations were

carried out using resources at the Center for High Performance Computing in Cape Town, South Africa.

REFERENCES

- Agertz O. et al., 2007, *MNRAS*, 380, 963
- Bahé Y. M., McCarthy I. G., 2015, *MNRAS*, 447, 969
- Bahé Y. M., McCarthy I. G., Balogh M. L., Font A. S., 2013, *MNRAS*, 430, 3017
- Bamford S. P. et al., 2009, *MNRAS*, 393, 1324
- Beck A. M. et al., 2016, *MNRAS*, 455, 2110
- Behroozi P. S., Wechsler R. H., Conroy C., 2013, *ApJ*, 770, 57
- Bernardi M., Meert A., Sheth R. K., Vikram V., Huertas-Company M., Mei S., Shankar F., 2013, *MNRAS*, 436, 697
- Biffi V., Sembolini F., De Petris M., Valdarnini R., Yepes G., Gottlöber S., 2014, *MNRAS*, 439, 588
- Booth C. M., Schaye J., 2009, *MNRAS*, 398, 53
- Borgani S., Kravtsov A., 2011, *Adv. Sci. Lett.*, 4, 204
- Boselli A., Gavazzi G., 2006, *PASP*, 118, 517
- Cen R., Ostriker J., 1992, *ApJ*, 393, 22
- Crain R. A. et al., 2009, *MNRAS*, 399, 1773
- Cui W. et al., 2016, *MNRAS*, 456, 2566
- Cybulski R., Yun M. S., Fazio G. G., Gutermuth R. A., 2014, *MNRAS*, 439, 3564
- Dalla Vecchia C., Schaye J., 2012, *MNRAS*, 426, 140
- Di Matteo T., Springel V., Hernquist L., 2005, *Nature*, 433, 604
- Dressler A., 1980, *ApJ*, 236, 351
- Elahi P. J., Thacker R. J., Widrow L. M., 2011, *MNRAS*, 418, 320
- Elahi P. J. et al., 2016, *MNRAS*, 458, 1096 (E16)
- Frenk C. S. et al., 1999, *ApJ*, 525, 554
- Fujita Y., 2004, *PASJ*, 56, 29
- Gill S. P. D., Knebe A., Gibson B. K., 2005, *MNRAS*, 356, 1327
- Gingold R. A., Monaghan J. J., 1977, *MNRAS*, 181, 375
- Gómez P. L. et al., 2003, *ApJ*, 584, 210
- Hahn O., Martizzi D., Wu H.-Y., Evrard A. E., Teyssier R., Wechsler R. H., 2015, *MNRAS*, preprint ([arXiv:1509.04289](https://arxiv.org/abs/1509.04289))
- Hirschmann M., Dolag K., Saro A., Bachmann L., Borgani S., Burkert A., 2014, *MNRAS*, 442, 2304
- Hogg D. W. et al., 2004, *ApJ*, 601, L29
- Hopkins P. F., Kereš D., Oñorbe J., Faucher-Giguère C.-A., Quataert E., Murray N., Bullock J. S., 2014, *MNRAS*, 445, 581
- Just D. W. et al., 2015, *ApJ*, preprint ([arXiv:1506.02051](https://arxiv.org/abs/1506.02051))
- Kim J.-h. et al., 2014, *ApJS*, 210, 14
- Klypin A., Kravtsov A. V., Bullock J. S., Primack J. R., 2001, *ApJ*, 554, 903
- Klypin A. A., Trujillo-Gomez S., Primack J., 2011, *ApJ*, 740, 102
- Knebe A. et al., 2011, *MNRAS*, 415, 2293
- Komatsu E. et al., 2011, *ApJS*, 192, 18
- Kravtsov A. V., Klypin A. A., Khokhlov A. M., 1997, *ApJS*, 111, 73
- Kravtsov A., Vikhlinin A., Meshcheryakov A., 2014, *ApJ*, preprint ([arXiv:1401.7329](https://arxiv.org/abs/1401.7329))
- Lewis I. et al., 2002, *MNRAS*, 334, 673
- Lucy L. B., 1977, *AJ*, 82, 1013
- McCarthy I. G., Schaye J., Bird S., Le Brun A. M. C., 2016, *MNRAS*, preprint ([arXiv:1603.02702](https://arxiv.org/abs/1603.02702))
- McGee S. L., Balogh M. L., Bower R. G., Font A. S., McCarthy I. G., 2009, *MNRAS*, 400, 937
- Onions J. et al., 2013, *MNRAS*, 429, 2739
- O’Shea B. W., Nagamine K., Springel V., Hernquist L., Norman M. L., 2005, *ApJS*, 160, 1
- Pearce F. R., Thomas P. A., Couchman H. M. P., Edge A. C., 2000, *MNRAS*, 317, 1029
- Pike S. R., Kay S. T., Newton R. D. A., Thomas P. A., Jenkins A., 2014, *MNRAS*, 445, 1774
- Piontek F., Steinmetz M., 2011, *MNRAS*, 410, 2625
- Poggianti B. M. et al., 2006, *ApJ*, 642, 188
- Prada F., Klypin A. A., Cuesta A. J., Betancort-Rijo J. E., Primack J., 2012, *MNRAS*, 423, 3018
- Rafieferantsoa M., Davé R., Anglés-Alcázar D., Katz N., Kollmeier J. A., Oppenheimer B. D., 2015, *MNRAS*, 453, 3980
- Read J. I., Hayfield T., Agertz O., 2010, *MNRAS*, 405, 1513
- Scannapieco C. et al., 2012, *MNRAS*, 423, 1726
- Schaye J., Dalla Vecchia C., 2008, *MNRAS*, 383, 1210
- Schaye J. et al., 2010, *MNRAS*, 402, 1536
- Schaye J. et al., 2015, *MNRAS*, 446, 521
- Sembolini F., Yepes G., De Petris M., Gottlöber S., Lamagna L., Comis B., 2013, *MNRAS*, 429, 323
- Sembolini F., De Petris M., Yepes G., Foschi E., Lamagna L., Gottlöber S., 2014, *MNRAS*, 440, 3520
- Sembolini F. et al., 2016a, *MNRAS*, in press
- Sembolini F. et al., 2016b, *MNRAS*, in press
- Springel V., 2010a, *ARA&A*, 48, 391
- Springel V., 2010b, *MNRAS*, 401, 791
- Springel V., Hernquist L., 2003, *MNRAS*, 339, 289 (SH03)
- Springel V. et al., 2005, *Nature*, 435, 629
- Stone J. M., Norman M. L., 1992, *ApJS*, 80, 753
- Tasker E. J., Brunino R., Mitchell N. L., Michielsen D., Hopton S., Pearce F. R., Bryan G. L., Theuns T., 2008, *MNRAS*, 390, 1267
- Teyssier R., 2002, *A&A*, 385, 337
- Teyssier R., Moore B., Martizzi D., Dubois Y., Mayer L., 2011, *MNRAS*, 414, 195
- Vogelsberger M., Genel S., Sijacki D., Torrey P., Springel V., Hernquist L., 2013, *MNRAS*, 436, 3031
- Vogelsberger M. et al., 2014, *MNRAS*, 444, 1518
- Wiersma R. P. C., Schaye J., Smith B. D., 2009, *MNRAS*, 393, 99

¹*School of Physics and Astronomy, University of Nottingham, Nottingham NG7 2RD, UK*

²*Sydney Institute for Astronomy, A28 School of Physics, The University of Sydney, NSW 2006, Australia*

³*International Centre for Radio Astronomy Research, University of Western Australia, 35 Stirling Highway, Crawley, WA 6009, Australia*

⁴*Departamento de Física Teórica, Módulo 8, Facultad de Ciencias, Universidad Autónoma de Madrid, E-28049 Madrid, Spain*

⁵*Astro-UAM, UAM, Unidad Asociada*

⁶*University Observatory Munich, Scheinerstr. 1, D-81679 Munich, Germany*

⁷*ARC Centre of Excellence for All-Sky Astrophysics*

⁸*Physics Department, University of the Western Cape, Cape Town 7535, South Africa*

⁹*South African Astronomical Observatory, PO Box 9, Observatory, Cape Town 7935, South Africa*

¹⁰*African Institute of Mathematical Sciences, Muizenberg, Cape Town 7945, South Africa*

¹¹*Center for High Performance Computing, CSIR Campus, 15 Lower Hope Street, Rosebank, Cape Town 7701, South Africa*

¹²*Astronomy Department, University of Massachusetts, Amherst, MA 01003, USA*

¹³*Jodrell Bank Centre for Astrophysics, School of Physics and Astronomy, The University of Manchester, Manchester M13 9PL, UK*

¹⁴*Astrophysics Research Institute, Liverpool John Moores University, 146 Brownlow Hill, Liverpool L3 5RF, UK*

¹⁵*INAF, Osservatorio Astronomico di Trieste, via G.B. Tiepolo 11, I-34143 Trieste, Italy*

¹⁶*Institute for Computational Science, ETH Zurich, Wolfgang-Pauli-Strasse 16, CH-8093 Zurich, Switzerland*

¹⁷*Institute of Astronomy and Kavli Institute for Cosmology, University of Cambridge, Madingley Road, Cambridge CB3 0HA, UK*

¹⁸*Department of Physics, Ludwig-Maximilians-Universität, Scheinerstr. 1, D-81679 München, Germany*

¹⁹*Institute of Theoretical Physics, Universität Zürich, Winterthurerstrasse 190, CH-8057 Zürich, Switzerland*